











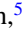



## Location and morphology of ferromagnetic precipitates in Ni-Mn-Sn

Nicolas Josten <sup>1,\*</sup>, Steffen Franzka <sup>2</sup>, Ziyuan Rao <sup>3</sup>, Tatiana Smoliarova <sup>1</sup>, András Kovács <sup>4</sup>,  
 Franziska Scheibel <sup>5</sup>, Franziska Staab <sup>6</sup>, Mehmet Acet <sup>1</sup>, Aslı Çakır <sup>7</sup>, Karsten Durst <sup>6</sup>, Baptiste Gault <sup>3,8</sup>,  
 Rafal E. Dunin-Borkowski <sup>4</sup>, Oliver Gutfleisch <sup>5</sup>, and Michael Farle <sup>1</sup>

<sup>1</sup>Faculty of Physics and Center for Nanointegration (CENIDE), University Duisburg Essen, Duisburg, 47057, Germany

<sup>2</sup>Interdisciplinary Center for Analytics on the Nanoscale (ICAN), Carl-Benz-Straße 199, 47057 Duisburg, Germany

<sup>3</sup>Max-Planck-Institut für Eisenforschung, Max-Planck-Strasse 1, Düsseldorf 40237, Germany

<sup>4</sup>Ernst Ruska-Centre for Microscopy and Spectroscopy with Electrons and Peter Grünberg Institute, Forschungszentrum Jülich, Jülich 52425, Germany

<sup>5</sup>Functional Materials, Institute of Materials Science, Technical University of Darmstadt, Peter-Grünberg-Str. 16, 64287 Darmstadt, Germany

<sup>6</sup>Physical Metallurgy, Institute of Materials Science, Technical University of Darmstadt, Peter-Grünberg-Str. 2, 64287 Darmstadt, Germany

<sup>7</sup>Department of Metallurgical and Materials Engineering, Mugla University, 48000 Mugla, Turkey

<sup>8</sup>Department of Materials, Imperial College, Royal School of Mines, London SW7 2AZ, United Kingdom



(Received 18 August 2023; accepted 21 November 2023; published 26 December 2023)

$\text{Ni}_{50}\text{Mn}_{45}\text{Sn}_5$  heated above 600 K decomposes into ferromagnetic  $\text{Ni}_2\text{MnSn}$  precipitates in an antiferromagnetic  $\text{NiMn}$  matrix. If an external magnetic field is applied during annealing, magnetic hysteresis curves with high coercive fields of up to 5 T can be achieved. The origin of this hysteresis has been attributed to the coupling of the antiferromagnetic matrix with the ferromagnetic precipitates, whose location and morphology were not known. To close this knowledge gap, four samples with varying annealing treatments were investigated using switching magnetization magnetic force microscopy. One sample was additionally analyzed with transmission electron microscopy and atom probe tomography. The decomposition type is identified to be a cellular precipitation starting at grain boundaries and growing into the grains. This leads to a multilayer thin film like lamellar structure with a lamella thickness in the nm range. Our results provide a basis for understanding the magnetic interactions, which lead to the magnetic hysteresis with ultra high coercivity.

DOI: [10.1103/PhysRevMaterials.7.124411](https://doi.org/10.1103/PhysRevMaterials.7.124411)

### I. INTRODUCTION

$\text{Ni}_{50}\text{Mn}_{50-x}\text{Sn}_x$  in the range of  $0 \leq x \leq 25$  changes structurally with increasing Sn content from tetragonal  $L1_0$  to the modulated structures 14M, 10M, and 4O, and finally to cubic  $L2_1$  [1,2]. The system is known for its martensitic transition and the tunability of its transition temperature by varying  $x$  [3], resulting in many different functionalities with the magnetocaloric effect being the most prominent [3–5].

Ni-Mn-Sn within this compositional range decomposes into  $L2_1$   $\text{Ni}_2\text{MnSn}$  and  $L1_0$   $\text{NiMn}$  when heated above 600 K [6–9].  $\text{Ni}_2\text{MnSn}$  is a ferromagnetic (FM) full Heusler with a Curie temperature  $T_C$  of 344 K [10].  $\text{NiMn}$ , on the other hand, is antiferromagnetic (AF) with an estimated Néel temperature  $T_N$  of 1070 K, which is unattainable due to a martensitic transition from  $L1_0$  to B2 at around 1000 K [11]. This decomposition also occurs in other Ni-Mn-X alloys (X: Al, Ga, In, and Sb) [12–14].

A common procedure to investigate this decomposition process is to anneal a sample and subsequently cool it below the decomposition temperature. It was shown that applying a magnetic field during annealing leads to a vertical shift of the magnetic hysteresis  $M(B)$ , i.e., a shift along the magnetization axis, which has been explained by the existence of strongly pinned magnetic moments. This has come to be known as the shell-ferromagnetic effect [9,15]. The vertical shift is often measured above the  $\text{Ni}_2\text{MnSn}$  Curie temperature to eliminate the spontaneous ferromagnetic contribution to  $M(B)$ . Increasing the annealing field and measurement range of  $M(B)$  to 14 T revealed that the vertical shift at least partly results from a magnetic hysteresis with an ultra high coercive field of 5 T [16], due to the interaction between the  $\text{NiMn}$  matrix and the  $\text{Ni}_2\text{MnSn}$  precipitates.

To fully understand this interaction, the morphological changes caused by the decomposition process need to be understood, specifically the shape, size, and location of the  $\text{Ni}_2\text{MnSn}$  precipitates inside the  $\text{NiMn}$  matrix. Previous x-ray based Scherrer analysis on a similar compound ( $\text{Ni}_{48}\text{Mn}_{47}\text{In}_{05}$ ) determined an average size of the precipitates of less than 50 nm [17]. Transmission electron microscopy (TEM) measurements on decomposed  $\text{Ni}_{50}\text{Mn}_{50-x}\text{Sn}_x$  ( $x = 11, 13, \text{ and } 15$ ) revealed a lamellar structure of the precipitates, but no decomposition mechanism has been specified [7,8].

\*Nicolas.Josten@uni-due.de

Published by the American Physical Society under the terms of the Creative Commons Attribution 4.0 International license. Further distribution of this work must maintain attribution to the author(s) and the published article's title, journal citation, and DOI.

TABLE I. Tabular list of the structure and composition of phase I and phase II.

Name	Structure	Composition
Phase I	L1 <sub>0</sub>	Ni <sub>51</sub> Mn <sub>44</sub> Sn <sub>05</sub>
Phase II	FCC	Ni <sub>58</sub> Mn <sub>40</sub> Sn <sub>02</sub>

The aim of this study is to determine the location and morphology of the Ni<sub>2</sub>MnSn precipitates inside the NiMn matrix. For this purpose, we use atomic force microscopy (AFM), magnetic force microscopy (MFM) adopting the switching magnetization MFM (SM-MFM) technique, TEM, and atom probe tomography (APT).

## II. EXPERIMENTAL

Two batches (batch A and batch B) of Ni-Mn-Sn with a nominal composition of Ni<sub>50</sub>Mn<sub>45</sub>Sn<sub>05</sub> were prepared by arc melting of pure elements ( $\geq 99.98\%$ ). The batches were subsequently encapsulated in a quartz tube under argon atmosphere and homogenized for five days at 1073 K. Afterwards, both were quenched in water at room temperature. Energy-dispersive x-ray spectroscopy (EDX) in a scanning electron microscope (SEM) showed that both batches consist of two phases: L1<sub>0</sub> Ni<sub>51</sub>Mn<sub>44</sub>Sn<sub>05</sub> (phase I), and a Ni-rich FCC phase with a composition of Ni<sub>58</sub>Mn<sub>40</sub>Sn<sub>02</sub> (phase II). The compositions are the same for both batches. The occurrence of phase II is due to a slight enrichment of Ni in the sample, which can occur due to the high volatility of Mn during arc melting. It had already been observed in the past [18,19]. The structure and composition of phase I and phase II are listed in Table I.

For magnetization measurements, a millimeter-sized cuboid was cut from batch A. The measurements were done in a Quantum Design PPMS DynaCool using a vibrating sample magnetometer (VSM). For magnetic annealing, the sample was mounted on a Quantum Design VSM oven heater stick using ceramic-based Zircar cement. The results are given in Appendix A.

For the investigation of the decomposition process, batch A and batch B were each cut into two pieces. One of the pieces was kept in its initial state (batch A). The others were annealed for 24 h at 650 K (batch B), 700 K (batch B), and 750 K (batch A) encapsulated in quartz tubes under argon atmosphere. Afterwards, they were polished with 3  $\mu\text{m}$ , 1  $\mu\text{m}$ , and 0.25  $\mu\text{m}$  diamond suspension. The final polishing was done with a colloidal silica suspension OP-U mixed 1:1 with water.

The optical micrographs were taken in brightfield incident light under slightly misaligned cross-polarization with an Olympus BX51TF optical microscope.

Surface topography was investigated by AFM measurements performed in air at 20–30% relative humidity using a Bruker Dimension Icon AFM in tapping mode. The scan rate was 0.5 Hz and 1024 samples per line were acquired. A MESP-LM-V2 cantilever (nom. resonant frequency: 75 kHz, nom. spring constant: 3 Nm<sup>-1</sup>, nom. tip radius: 25 nm, Bruker, USA) was used. The tip itself has a nom. magnetic moment of  $3 \times 10^{-17} \text{Am}^2$ . Image analysis was performed using NanoScope Analysis 1.9 (Bruker, USA). The images

were flattened and eventually low pass filtered to remove high frequency noise.

The MFM measurements were carried out in lift mode according to the method of SM-MFM [20–22], where a reversal of the tip magnetization leads to an opposite shift of the MFM phase signal. The difference of two MFM phase signals obtained for opposite tip magnetizations (north and south), which we call the  $\Delta\text{MFM}$  phase, eliminates nonmagnetic contributions in the MFM scans (for details see Appendix B). The lift height of the tip during the measurements was 20 nm. The spatial resolution of the AFM/MFM measurements is about 50 nm.

EDX mapping in an SEM was used to determine the spatially resolved composition of the SM-MFM measurement areas.

TEM measurements were performed in an aberration-corrected transmission electron microscope (FEI Titan G2 60-200) equipped with in-column EDX detectors. The electron transparent specimen with a thickness of approximately 50 nm was prepared using a focused ion beam (FIB) inside a dual-beam FIB/SEM system (FEI Helios NanoLab 460F1). EDX measurements inside the TEM were analyzed with a standardless Cliff-Lorimer quantification resulting in an estimated error of 10%.

APT measurements were carried out using a Cameca Inc. LEAP 5000X HR device. For this, a tip was prepared by the FIB method using a FEI Helios Nanolab 600i system. The tip has a height of around 235 nm and a base radius of around 55 nm.

## III. RESULTS

### A. Microstructure

Light microscopy images of the initial state sample and the samples which were annealed for 24 h at 650 K, 700 K, and 750 K are shown in Fig. 1 (the squares highlight areas used for SM-MFM measurements in Sec. III B). The initial state shows the typical martensitic microstructure which is expected for this composition [3,18]. The microstructure consists of martensitic plates, which appear as stripes and can be identified by their light-dark contrast. They belong to phase I and their boundaries are twin boundaries [23]. These martensitic plates form domains with sizes varying from a few microns up to hundreds of microns. Other features in the microstructure are pores, which appear as black spots, and micrometer-sized inclusions of phase II. The latter two can be found in all four samples and are highlighted for the 750 K annealed sample in Fig. 1(d).

The microstructure of the sample annealed at 650 K appears similar to that of the initial state. Differences in the size of the martensitic plates and domains between those of the initial state and the 650 K state are due to grain size variations within the samples. No phase decomposition is observable.

For the sample annealed at 700 K, major structural changes occur. Next to the martensitic microstructure of phase I and the micrometer-sized inclusions of phase II, an additional phase decomposition of phase I into Ni<sub>2</sub>MnSn and NiMn is observed. The resulting nanocomposite is highlighted with black/white striped lines in Fig. 1(c) and is limited to the grain boundaries.

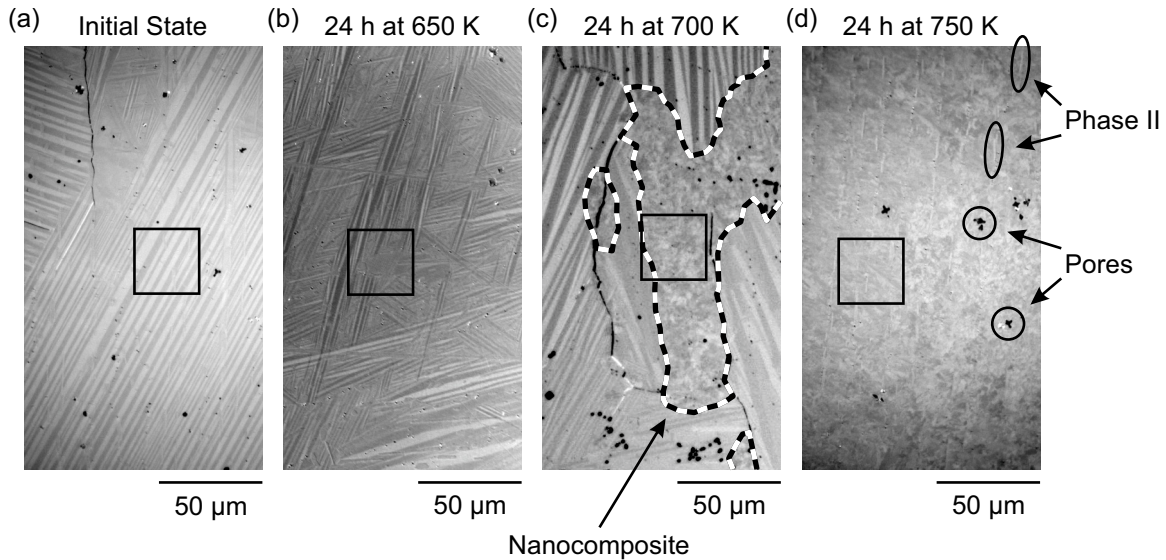


FIG. 1. Reflected light microscopy images of the polished sample surfaces taken with a polarization filter. (a) The initial state and the samples, which were annealed for 24 h at (b) 650 K, (c) 700 K, and (d) 750 K are shown. The  $30\ \mu\text{m} \times 30\ \mu\text{m}$  black squares highlight areas on which AFM and SM-MFM measurements were done. The black/white striped lines in (c) surround areas in which the sample is decomposed and forms a nanocomposite. In (d) the micrometer-sized inclusions of phase II and the pores, which are present in all four samples, are circled.

For the sample annealed at 750 K, phase I and its martensitic microstructure are not observable anymore. The sample is now largely decomposed. The micrometer-sized inclusions of phase II, on the other hand, are still present.

Figure 2 shows the spatially resolved composition of all four samples measured by EDX mapping (the squares again highlight areas used for SM-MFM measurements in Sec. III B). The EDX mapping allows to distinguish phase I with a composition of  $\text{Ni}_{51}\text{Mn}_{44}\text{Sn}_{05}$ , and phase II with a composition of  $\text{Ni}_{58}\text{Mn}_{40}\text{Sn}_{02}$ . This means that phase II can be distinguished from phase I by its increased amount of Ni (bright red) with a simultaneous decrease of Sn (dark green). The EDX mapping of phase I does not change after annealing despite the progressing decomposition. The resolution of the EDX mapping does not allow to resolve the nanometer-sized precipitates in the 700 K and 750 K annealed samples. Phase II exists in all samples as micrometer-sized inclusions in phase I.

The pores, one of which is visible on the right side of the EDX mapping of the initial state sample in Fig. 2, are coated with MnO.

### B. Magnetic force microscopy

In Fig. 3, AFM and SM-MFM measurements on all four samples are presented. For this, a  $30\ \mu\text{m} \times 30\ \mu\text{m}$  area was chosen on each sample. These areas are highlighted by squares in the micrographs in Figs. 1 and 2.

The topography images in Figs. 3(a), 3(c), 3(e), and 3(g) complement the microscopy and SEM images of the microstructure. For the initial state and the 650 K sample, the twinned martensitic plates of phase I are visible as faint light and dark parallel stripes. For the 700 K and 750 K samples, no single grains can be identified in the topography since the areas essentially show only the nanocomposite resulting from

the decomposition. For all four samples, the micrometer-sized inclusions of phase II protrude from the surface as elevated structures. The topography images show that phase II is also affected by the annealing, as can be seen by comparing the initial state [Fig. 3(a)] with the 750 K sample [Fig. 3(g)]. Here, the boundary between phase I and phase II becomes more irregular with increasing annealing temperature.

The SM-MFM measurements show the spatially resolved  $|\Delta\text{MFM phase}|$ , which is the absolute difference of the two MFM phase measurements with opposite tip magnetization. With this technique, it is possible to visualize the decomposition of Ni-Mn-Sn into  $\text{Ni}_2\text{MnSn}$  and NiMn. Since  $\text{Ni}_2\text{MnSn}$  is FM, its precipitates produce a magnetic stray field. A nanocomposite consisting of FM  $\text{Ni}_2\text{MnSn}$  and AF NiMn therefore produces mosaic areas, in which large and small magnetic fields alternate. An area with a large stray field does not necessarily indicate a single ferromagnetic particle. This method is, therefore, only suitable to visualize the rough spatial distribution of the magnetic precipitates without resolving the shape of any individual precipitate.

In the SM-MFM measurements of the initial state [Fig. 3(b)], no magnetic contrast can be seen. This is expected for the not-decomposed sample [3,24].

In the sample annealed at 650 K [Fig. 3(d)], magnetic contrast is visible at the grain boundary. The martensitic plates and their twin boundaries, on the other hand, show no magnetic contrast. The magnetic origin of this contrast is confirmed in Appendix B by additional magnetizing of the sample.

For the 700 K sample [Fig. 3(f)], the SM-MFM measurements show a part of the decomposed area highlighted in Fig. 1(c). At the bottom left of Fig. 3(f), the measurement area includes remaining parts of the original martensitic microstructure. The nanocomposite shows a fine mosaic contrast, which is the expected result for nanometer-sized ferromagnetic precipitates in an antiferromagnetic matrix. The

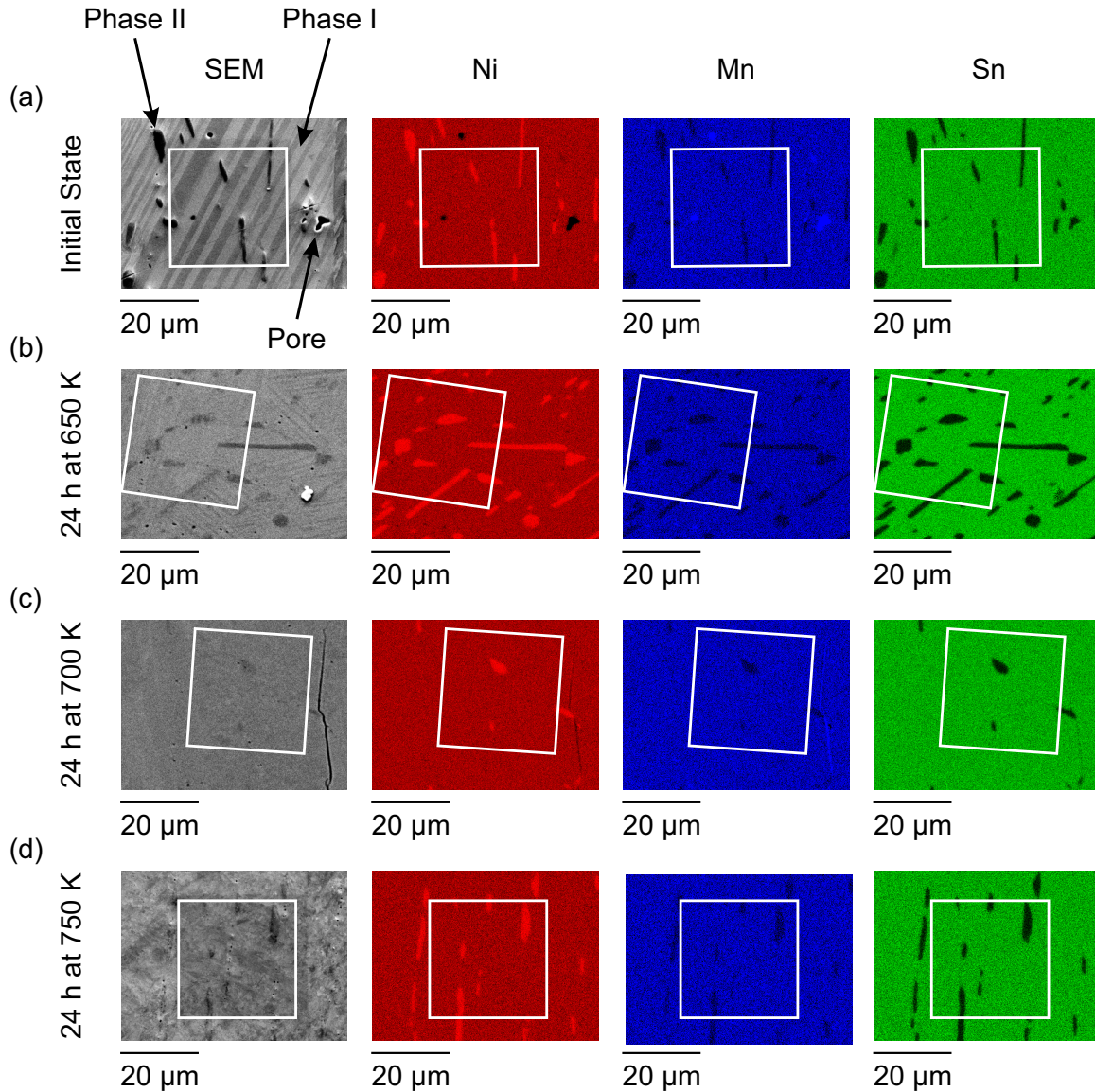


FIG. 2. SEM images and EDX mapping of the polished sample surfaces in the initial state and after annealing for 24 h at 650 K, 700 K, and 750 K. The  $30\ \mu\text{m} \times 30\ \mu\text{m}$  white squares highlight areas, on which AFM and SM-MFM measurements were done. The EDX mappings show the elemental distributions of Ni, Mn, and Sn. Most of the sample consists of phase I with a composition of  $\text{Ni}_{51}\text{Mn}_{44}\text{Sn}_{05}$ . The micrometer-sized precipitates of phase II can be identified by their increased Ni and decreased Sn content. The composition of phase II is  $\text{Ni}_{58}\text{Mn}_{42}\text{Sn}_{02}$ . Other features on the sample surface are pores, which are covered by MnO and can thus be identified in the EDX mapping as an increased amount of Mn.

mosaic magnetic structure includes two islands with no magnetic contrast. The locations match with the position of phase II in Fig. 2(c). The original martensitic microstructure of phase I on the bottom left, which is not yet decomposed, also shows no magnetic contrast.

The microstructure of the 750 K sample revealed that this sample is essentially decomposed. Accordingly, the SM-MFM measurements [Fig. 3(h)] show that the measurement area consists of the mosaic magnetic structure. Only the islands of phase II can still be distinguished. The increased darkness with increasing annealing temperature reflects the increasing amount of ferromagnetic material in the sample.

### C. Transmission electron microscopy

TEM measurements were performed on a lamella, which was cut from the nanocomposite in Fig. 1(c). The results are shown in Fig. 4.

Figure 4(a) is a high-angle annular dark-field (HAADF) scanning transmission electron microscopy (STEM) image of a decomposed region. It shows a lamellar structure with colonies of alternating bright and dark layers. The yellow square in Fig. 4(a) is analyzed in more detail with a HAADF image in Fig. 4(b) and EDX mappings in Fig. 4(c). Here, the bright layers can be identified as the  $\text{Ni}_2\text{MnSn}$  precipitates, while the dark layers are NiMn. The thickness of the precipitates is around 10 nm. Figure 4(d) shows three EDX linescans

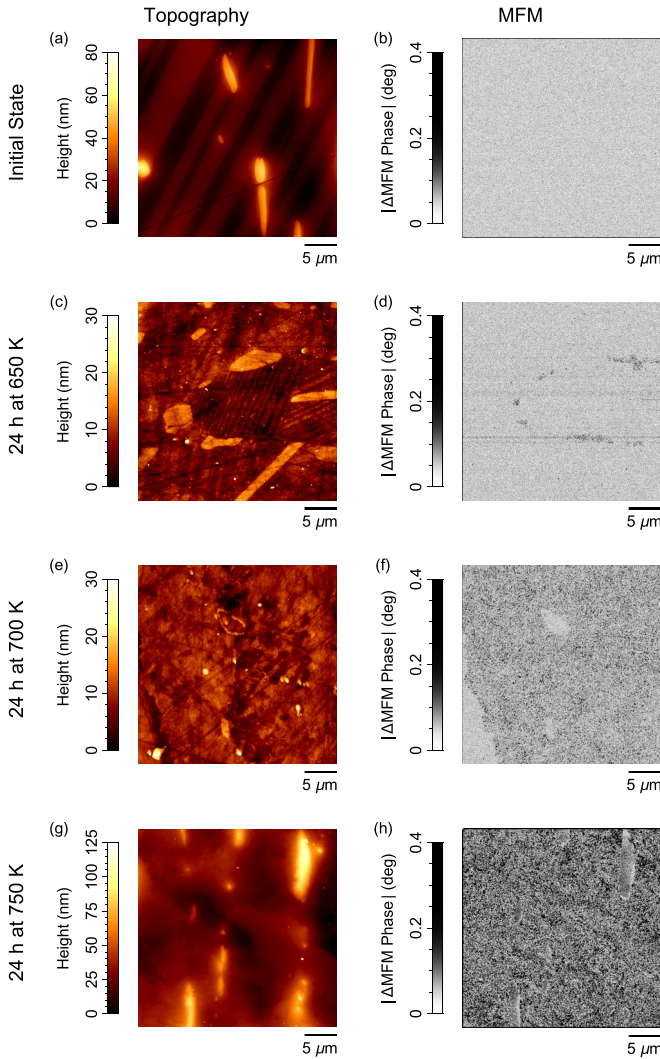


FIG. 3. AFM and SM-MFM measurements of the initial state and after annealing for 24 h at 650 K, 700 K, and 750 K. The measurement areas have dimensions of  $30 \mu\text{m} \times 30 \mu\text{m}$  and are highlighted with black squares in Fig. 1. For each annealing temperature the topography and the  $|\Delta\text{MFM phase}|$  are shown. The  $|\Delta\text{MFM phase}|$  is the absolute difference of two MFM phase measurements with opposite tip magnetization.

measured along the yellow rectangles shown in Fig. 4(b). The  $x$ -axes of the linescans follow the yellow arrows. The composition of the precipitates is approximately  $\text{Ni}_{52}\text{Mn}_{29}\text{Sn}_{19}$ , while the average composition of the matrix (dark layers) is  $\text{Ni}_{54}\text{Mn}_{44}\text{Sn}_{02}$ .

#### D. Atom probe tomography

To provide further information on the morphology and composition of the ferromagnetic precipitates, APT measurements were done on a tip which was cut from the nanocomposite seen in Fig. 1(c). Figure 5 shows the 3D APT tip reconstructions of (a) Ni, (b) Mn, and (c) Sn. The precipitates are best visible in the Sn reconstruction, which has the greatest relative change in composition between precipitates and matrix. Here, the precipitates are clearly visible as a lamellar structure. The tip shows a region in which two different

growth directions of the lamellae intersect. To improve the visibility of the precipitates, Fig. 5(d) only depicts regions with Sn concentrations  $\geq 8$  at%. In Fig. 5(e), this region is shown in combination with two red cylinders (A) and (B), each with a length of 30 nm and a diameter of 10 nm. Along the length direction of these cylinders, compositional profiles were determined and are shown in Fig. 5(f). A distance of 0 nm in this profile corresponds to the bottom end of the cylinders.

The composition of the precipitates is approximately  $\text{Ni}_{56}\text{Mn}_{31}\text{Sn}_{13}$ . At the same time, the surrounding matrix still contains some Sn with an average composition of  $\text{Ni}_{48}\text{Mn}_{49}\text{Sn}_{03}$ .

The morphology of the precipitates is in good agreement with the TEM results presented in Sec. III C. The composition, on the other hand, deviates with a significantly lower Sn concentration for the precipitates in the APT measurements. Apart from measurement errors and natural variations in composition, this can be explained with the measurement location. The measurement area investigated by TEM is within a colony, while the APT results show the intersection between two colonies. In the intersection, a less complete decomposition is expected with a lower amount of Sn in the precipitates.

#### IV. DISCUSSION

In an applied magnetic field, the decomposition of Ni-Mn-Sn into FM  $\text{Ni}_2\text{MnSn}$  and AF NiMn is accompanied by the emergence of a vertically shifted  $M(B)$  and a magnetic hysteresis with ultra high coercivity ([9,16], Appendix A). Various effects result in a shifted  $M(B)$  curve. The hysteresis can be a minor loop of a larger hysteresis [25], the hysteresis can be horizontally shifted due to exchange bias interactions [26], or the hysteresis can be vertically shifted due to strongly pinned or uncompensated magnetic moments [9,27]. The proposed model, known as the shell-ferromagnetic model, explains the vertical shift of  $M(B)$  and the magnetic hysteresis with ultra high coercivity with pinned magnetic moments at the interface (the eponymous shell) between FM precipitate and AF matrix [15]. The core of the precipitates is assumed to be soft magnetic below the Curie temperature of  $\text{Ni}_2\text{MnSn}$ . This model has been illustrated with spherical precipitates, however, no explicit shape was identified [16].

This work shows that the decomposition process is a cellular precipitation [28,29]. It leads to a lamellar structure, in which nm-sized FM and AF layers alternate. With Fig. 4 the thickness of the FM layers at an annealing temperature of 700 K can be estimated to lie around 10 nm. This configuration is reminiscent of AF-FM multilayer thin films, which are associated with exchange bias [30]. Exchange bias usually denotes the horizontal shift of a magnetic hysteresis due to the magnetic coupling between antiferromagnet and ferromagnet, and has already been discussed as a potential hardening mechanism for permanent magnets [31]. A recent study [32,33] based on our previous results [16] is able to reproduce the magnetic hysteresis with ultra high coercivity in mesoscopic magnetic simulations with a nanocomposite of AF and FM grains.

Exchange bias is mediated by uncompensated magnetic moments in the antiferromagnet [34]. These are often

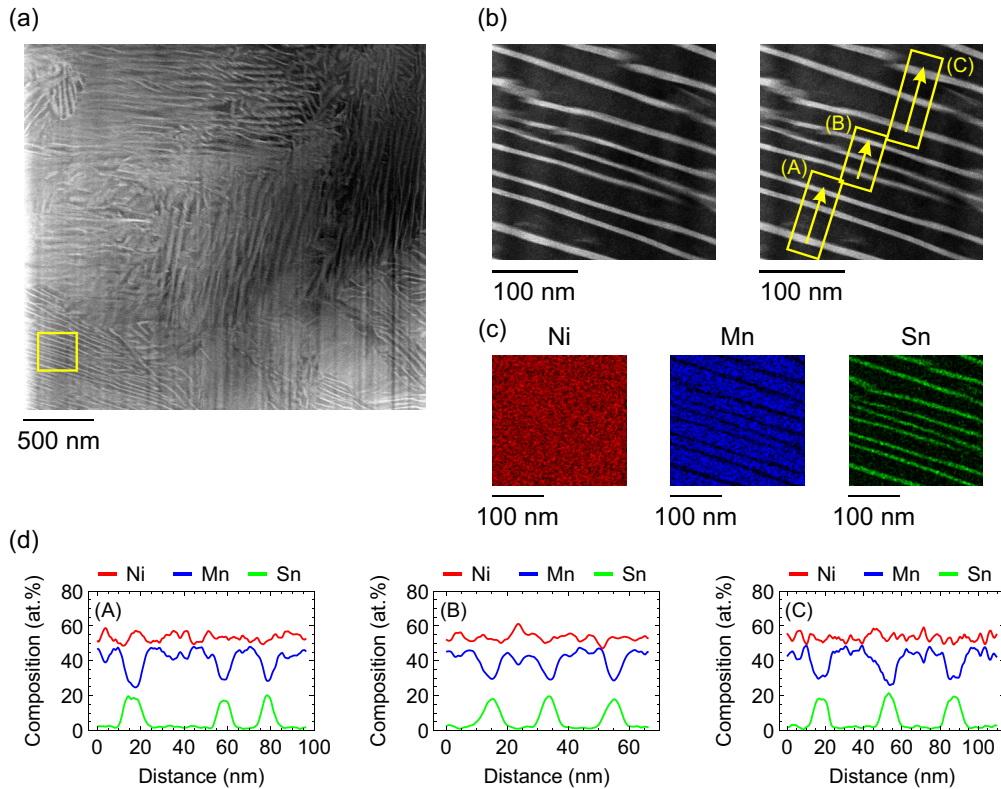


FIG. 4. (a) HAADF STEM image of the sample annealed for 24 h at 700 K. The decomposition product of phase I toward  $\text{Ni}_2\text{MnSn}$  and  $\text{NiMn}$  is visible and forms a lamellar structure. (b) HAADF STEM image of the region marked in (a) (yellow rectangle). The thickness of the  $\text{Ni}_2\text{MnSn}$  lamellar precipitates is around 10 nm. (c) EDX mappings of Ni, Mn, and Sn performed on the area shown in (b). (d) EDX linescans measured within the yellow rectangles shown in (b). The  $x$ -axes of the plots of the linescans follow the yellow arrows.

generated by cooling through the Néel temperature within an applied magnetic field [35] and are not necessarily limited to the interface region, but can instead be present throughout the antiferromagnet [36]. The theoretical Néel temperature of  $\text{NiMn}$  is estimated to be about 1070 K [11], which lies above its martensitic transition temperature of around 1000 K [37], and significantly above the annealing temperature of 650 K used to obtain the magnetic hysteresis with ultra high coercivity in Appendix A. Instead of cooling through the Néel temperature, uncompensated magnetic moments in  $\text{NiMn}$  with slight Ni excess can be generated by diffusion in an applied magnetic field [27,38]. This leads to a vertically shifted  $M(B)$ , similar to Ni-Mn-Sn in this work, while lacking the magnetic hysteresis with ultra high coercivity. This effect only works efficiently in a temperature range of  $\pm 50$  K around 650 K, which was demonstrated on  $\text{PdMn}$  [39]. This fits the annealing temperature used to obtain the magnetic hysteresis with ultra high coercivity in Ni-Mn-Sn.

The biggest hurdle, which needs to be overcome to use Ni-Mn-Sn as permanent magnets, is the low magnetization of the magnetic hysteresis with ultra high coercivity.  $\text{Ni}_2\text{MnSn}$  has a saturation magnetization at room temperature of around  $40 \text{ Am}^2\text{kg}^{-1}$  [3], which reduces to  $10 \text{ Am}^2\text{kg}^{-1}$  in fully decomposed  $\text{Ni}_{50}\text{Mn}_{45}\text{Sn}_{05}$ . Currently, only a fraction of this magnetization can be utilized for the magnetic hysteresis with ultra high coercivity. Among other things, this can be explained with the presence of different lamellar colonies within the sample, which can be seen in Fig. 4(a). These colonies

lead to various possible crystallographic orientations of the antiferromagnetic matrix with respect to the annealing field. It is known from exchange bias that the FM-AF coupling is strongly dependent on this orientation [40]. Accordingly, some precipitates can be strongly coupled to the surrounding antiferromagnet, while others can be decoupled and behave as normal soft magnetic  $\text{Ni}_2\text{MnSn}$ , which could be an alternative explanation for the soft and hard magnetic components visible in  $M(B)$  [16] in contrast to the shell-ferromagnetic model.

In the ideal case, all lamellae lie parallel to the annealing field with an optimal crystallographic orientation of the antiferromagnetic matrix. A similar microstructure has already been realized in Alnico [41], in which spinodal decomposition within a magnetic field leads to a favorable orientation of the FM  $\alpha_1$  phase. To achieve the same result in Ni-Mn-Sn will be difficult.  $\text{Ni}_2\text{MnSn}$  is not ferromagnetic at the annealing temperature, which prevents a favorable crystallographic orientation along the magnetic field during decomposition. Additionally, in cellular precipitation the crystallographic orientation of the product phase is identical to the parent phase [42]. This means a favorable crystallographic orientation has to be established before decomposition.

## V. CONCLUSION

In this work, the decomposition of  $\text{Ni}_{51}\text{Mn}_{44}\text{Sn}_{05}$  into ferromagnetic  $\text{Ni}_2\text{MnSn}$  and antiferromagnetic  $\text{NiMn}$  was studied at length scales from  $\mu\text{m}$  to nm. Four samples were

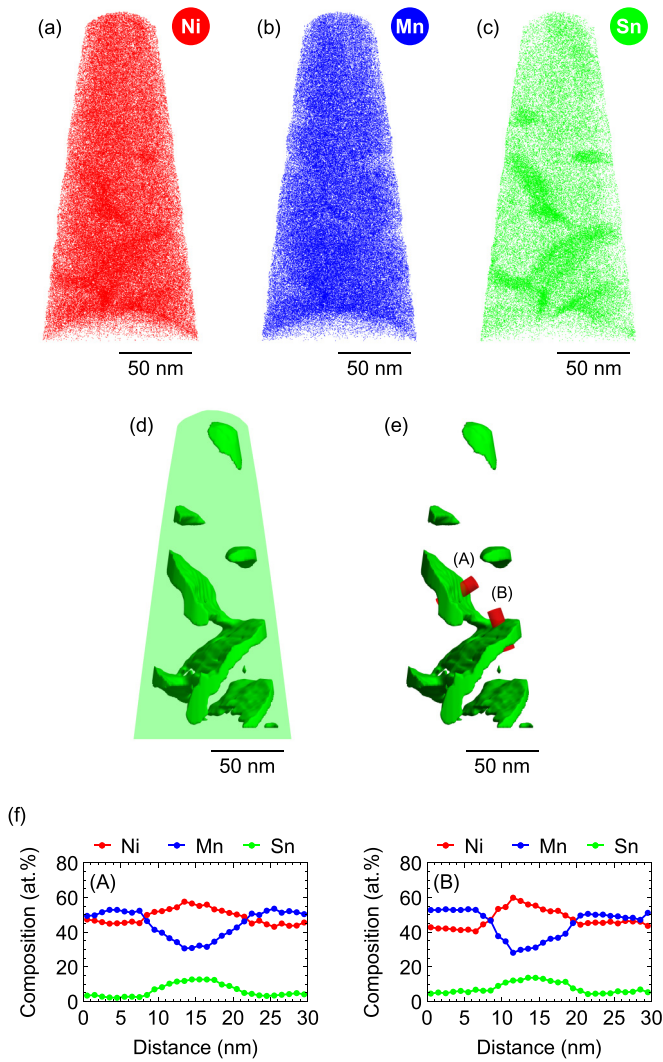


FIG. 5. APT analysis of the sample annealed for 24 h at 700 K. (a), (b), and (c) are 3D APT tip reconstructions of Ni, Mn, and Sn, respectively. (d) Regions with  $\geq 8$  at% Sn shown in 3D with the original size of the tip shown as green background. Only regions with more than 8 nm distance from the tip surface were evaluated. (e) Two red cylinders (A) and (B) with a length of 30 nm and a diameter of 10 nm crossing the precipitates. Along these cylinders, compositional profiles (f) were determined. A distance of 0 nm corresponds to the bottom the cylinders.

analyzed, of which three were annealed for 24 h at 650 K, 700 K, and 750 K. The analysis of the microstructure with light microscopy and SEM shows the gradual change with increasing annealing temperature from the martensitic initial state to a nanocomposite consisting of  $\text{Ni}_2\text{MnSn}$  and  $\text{NiMn}$ . The grain boundaries are the starting point of this decomposition. An additional cubic  $\text{Ni}_{58}\text{Mn}_{40}\text{Sn}_{02}$  phase in the sample is mostly unaffected by this decomposition.

With the help of TEM and APT, the decomposition process was identified as a cellular precipitation, which results in a lamellar structure with alternating layers of  $\text{Ni}_2\text{MnSn}$  and  $\text{NiMn}$ . The thickness of the  $\text{Ni}_2\text{MnSn}$  precipitates is around 10 nm after annealing for 24 h at 700 K.

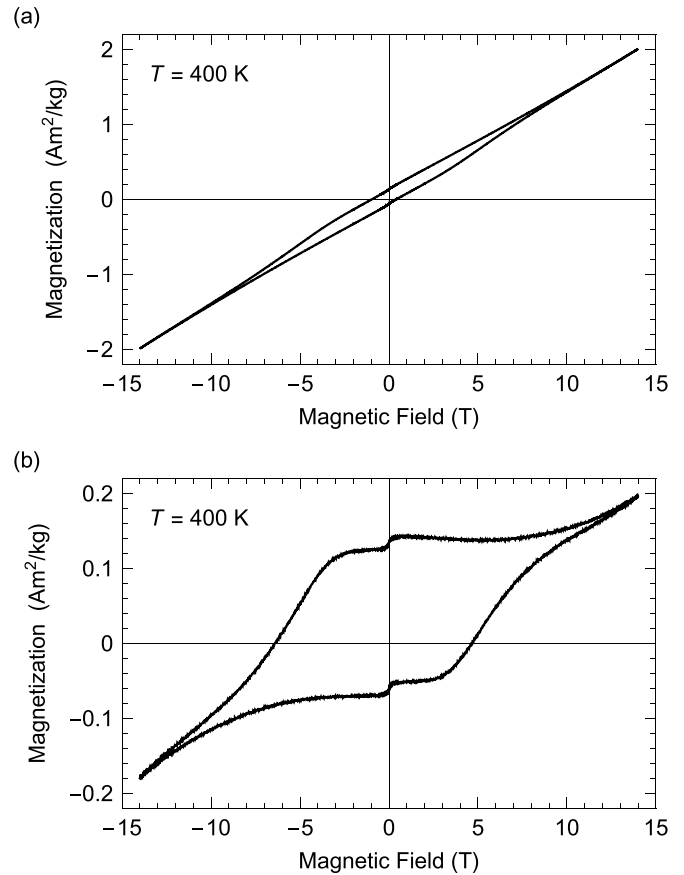


FIG. 6. (a)  $M(B)$  measured at 400 K after magnetic annealing for 6 h at 650 K with an applied magnetic field of 14 T. (b) The same  $M(B)$  curve after subtraction of the linear background of the antiferromagnet.

The motivation of this study is the presence of a hysteresis with coercive fields around 5 T after magnetic annealing at 650 K. In the discussion, the resulting lamellar structure is compared to exchange biased AF-FM multilayer thin films to explain the high coercivity. To use this material as a permanent magnet a larger magnetization is needed. For this, a better morphological and crystallographic orientation of the lamellae has to be achieved.

ACKNOWLEDGMENTS

We acknowledge funding by the German Research Foundation (DFG) within the Collaborative Research Center/Transregio (CRC/TRR) 270 (Project-No. 405553726, Subprojects A04, A08, B01, Z01, and Z02).

The authors are grateful to L. Kibkalo (ER-C Forschungszentrum Jülich) for specimen preparation.

APPENDIX A: MAGNETIC ANNEALING

Figure 6(a) shows the occurrence of a magnetic hysteresis with ultra high coercivity after magnetic annealing. Here, the  $M(B)$  curve of a cuboid cut from batch A is plotted at 400 K. The sample was previously annealed for 6 h at 650 K in an applied magnetic field of 14 T. The largest contribution

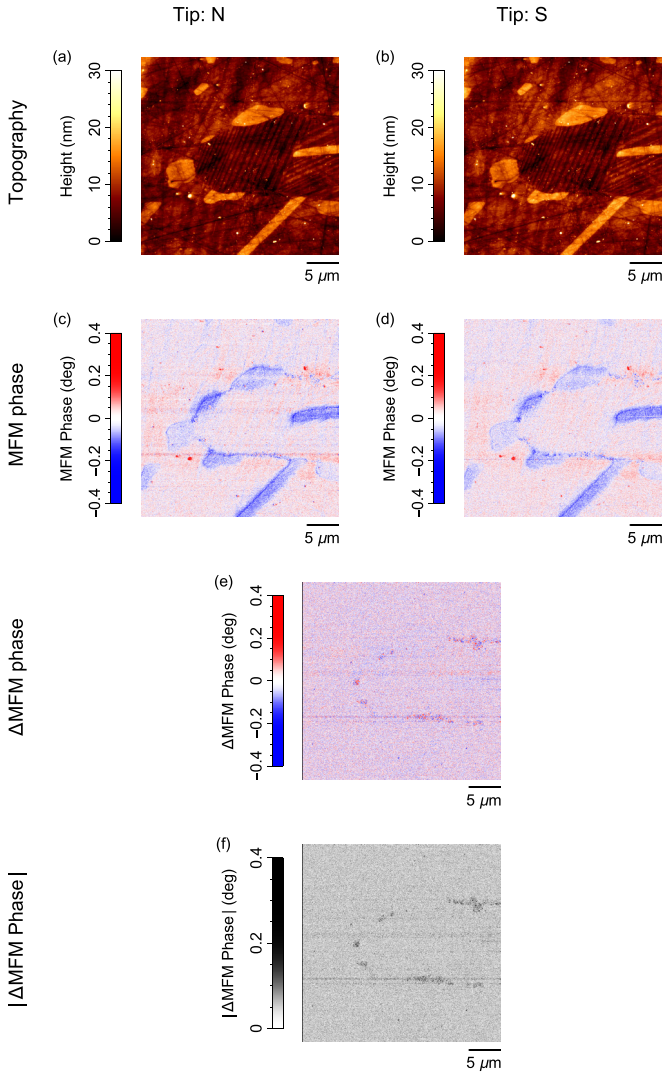


FIG. 7. AFM and MFM measurements of the sample annealing for 24 h at 650 K. The topography and MFM phase measurements are shown for both directions of the tip magnetization (north and south). The  $\Delta$ MFM phase is then the difference of both MFM phase measurements and can either be plotted with a diverging or a mirrored colormap.

to  $M(B)$  is a linear background coming from the predominantly AF material. This linear background was subtracted in Fig. 6(b). The curvature of  $M(B)$  at high fields, which becomes visible after subtraction of the linear background, is a nonlinear magnetic contribution of the antiferromagnet and is related to the high magnetocrystalline anisotropy.

The magnetic hysteresis with an ultra high coercive field greater than 5 T and other magnetic contributions were discussed in detail in Ref. [16].

## APPENDIX B: SWITCHING MAGNETIZATION MAGNETIC FORCE MICROSCOPY

SM-MFM is a special technique aimed to improve the contrast obtained by conventional MFM measurements. Historically, it was introduced during the development of the MFM technique to confirm the magnetic origin of the detected signals [20]. The main idea is that a reversal of the tip

TABLE II. Relationships of the magnetic part of the MFM-phase images for different sample and tip magnetizations. For all six unique combinations, two yield the same (1), while four yield an opposite (−1) magnetic part of the MFM-phase images.

MFM image 1		MFM image 2		Relation
Sample	Tip	Sample	Tip	
N	N	S	S	1
N	S	S	N	1
N	N	N	S	−1
N	N	S	N	−1
S	S	N	S	−1
S	S	S	N	−1

magnetization changes the sign of the magnetic contribution to the MFM phase signal [21,22]. Other contributions, like electric and atomic forces, do not have their signs changed. This means the difference of the two phase images obtained for opposite tip magnetizations will result in an enhancement of the magnetic contrast while simultaneously removing unwanted contributions. The SM-MFM technique is presented in Fig. 7 on measurements done on the sample annealed for 24 h at 650 K. First, the topography was measured [Fig. 7(a)]. Then, the tip was lifted, in this case by 20 nm, and followed the topography to measure the MFM phase [Fig. 7(c)]. This was repeated for the opposite tip magnetization [Figs. 7(b) and 7(d)]. The resulting MFM phase images are disturbed by nonmagnetic contributions to the measured MFM phase. They can be identified as identical features in both MFM phase measurements. These features mimic the topography of the sample, especially the elevated structures of phase II result in a large disturbance of the MFM phase, even though no magnetic stray field is expected for this phase [3,24]. These contributions can be removed by subtracting one MFM phase measurement from the other. Before this can be done, a possible drift of the measurement area between the two measurements has to be corrected by a translational shift of the image. The result of subtraction is the  $\Delta$ MFM phase showing the isolated magnetic contribution. In general, the information of the stray field direction is not lost and can be shown with a diverging color map as was done in Fig. 7(e). However, due to the small size of the precipitates, it is better to plot the absolute value  $|\Delta$ MFM phase| [Fig. 7(f)] as was done in the main text. The contrast of SM-MFM images can be enhanced by additionally magnetizing the sample prior to the measurements. Together with the tip magnetization, this results in four different combinations for the tip and sample magnetization (sample: N and tip: N; sample: S and tip: S; sample: N and tip: S; sample: S and tip: N). A normal SM-MFM image is generated as the difference between two MFM phase images obtained for opposite tip magnetizations. This definition can be expanded to include the sample magnetization, which leads to six unique combinations of two MFM phase images obtained for different variations of tip and sample magnetization. Two of these combinations have the same, and four an opposite magnetic part of the MFM phase signal. The different combinations are shown in Table II. The general rule is that reversing both the magnetization of the



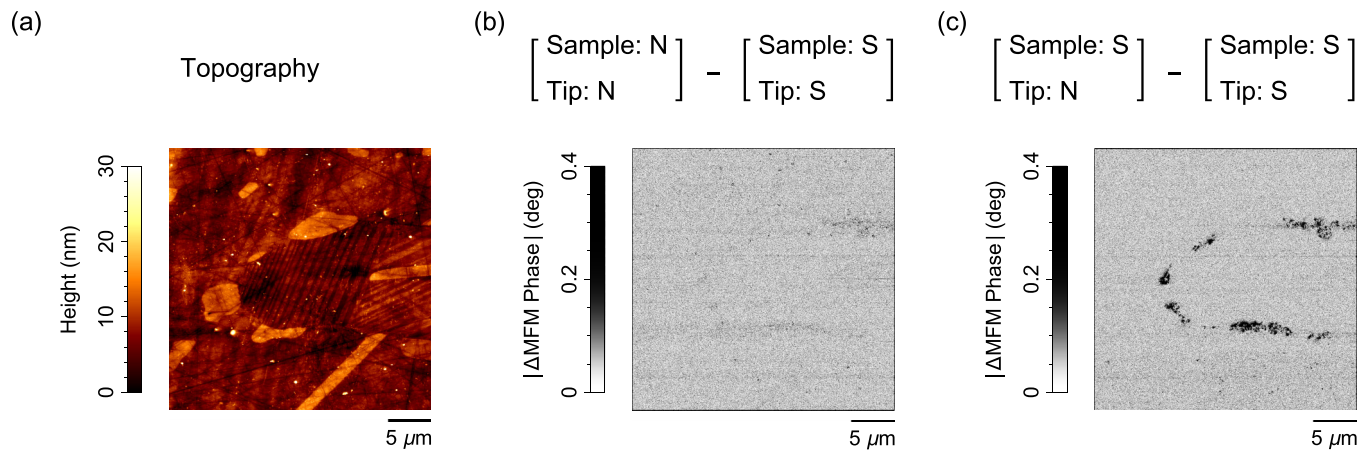


FIG. 8. AFM and SM-MFM measurements after annealing for 24 h at 650 K. The SM-MFM measurements show the  $|\Delta\text{MFM phase}|$  for different combinations of tip and sample magnetization. For the combination of sample: N and tip: N with sample: S and tip: S the same MFM-phase images are expected for both measurements and therefore cancel each other out. For the combination of sample: S and tip: N with sample: S and tip: S the MFM-phase images are expected to be opposites and therefore magnetic contrast is visible.

sample and the tip leads to the same, while reversing just one of the two leads to an opposite magnetic part of the MFM phase signal.

In Fig. 8 the results of SM-MFM measurements obtained by additional magnetizing of the sample are shown for the sample annealed for 24 h at 650 K. The measurement area is the same as in Fig. 7. Figure 8(a) shows the topography, while Figs. 8(b) and 8(c) show SM-MFM results for different com-

binations of sample and tip magnetization. If the difference of the MFM phase images are taken with both the magnetization of the sample and the tip reversed (e.g., sample: N, tip: N; sample: S, tip: S) the contrast disappears [Fig. 8(b)]. In the case that only the magnetization of the sample or the tip is reversed (e.g., sample: S, tip: N; sample: S, tip: S) the contrast increases [Fig. 8(c)]. This confirms the magnetic origin of the measured contrast.

- [1] X. Moya, L. Mañosa, A. Planes, T. Krenke, M. Acet, and E. F. Wassermann, Martensitic transition and magnetic properties in Ni-Mn-X alloys, *Mater. Sci. Eng.: A* **438–440**, 911 (2006).
- [2] H. Zheng, W. Wang, S. Xue, Q. Zhai, J. Frenzel, and Z. Luo, Composition-dependent crystal structure and martensitic transformation in Heusler Ni-Mn-Sn alloys, *Acta Mater.* **61**, 4648 (2013).
- [3] T. Krenke, M. Acet, E. F. Wassermann, X. Moya, L. Mañosa, and A. Planes, Martensitic transitions and the nature of ferromagnetism in the austenitic and martensitic states of Ni-Mn-Sn alloys, *Phys. Rev. B* **72**, 014412 (2005).
- [4] T. Krenke, E. Duman, M. Acet, E. F. Wassermann, X. Moya, L. Mañosa, and A. Planes, Inverse magnetocaloric effect in ferromagnetic Ni-Mn-Sn alloys, *Nat. Mater.* **4**, 450 (2005).
- [5] A. Planes, L. Mañosa, and M. Acet, Magnetocaloric effect and its relation to shape-memory properties in ferromagnetic Heusler alloys, *J. Phys.: Condens. Matter* **21**, 233201 (2009).
- [6] D. Schlagel, R. McCallum, and T. Lograsso, Influence of solidification microstructure on the magnetic properties of Ni-Mn-Sn Heusler alloys, *J. Alloys Compd.* **463**, 38 (2008).
- [7] W. M. Yuhasz, D. L. Schlagel, Q. Xing, K. W. Dennis, R. W. McCallum, and T. Lograsso, Influence of annealing and phase decomposition on the magnetostructural transitions in Ni<sub>50</sub>Mn<sub>39</sub>Sn<sub>11</sub>, *J. Appl. Phys.* **105**, 07A921 (2009).
- [8] W. Yuhasz, D. Schlagel, Q. Xing, R. McCallum, and T. Lograsso, Metastability of ferromagnetic Ni-Mn-Sn Heusler alloys, *J. Alloys Compd.* **492**, 681 (2010).
- [9] A. Çakır and M. Acet, Non-volatile high-temperature shell-magnetic pinning of Ni-Mn-Sn Heusler precipitates obtained by decomposition under magnetic field, *J. Magn. Magn. Mater.* **448**, 13 (2018).
- [10] P. J. Webster, Heusler alloys, *Contemp. Phys.* **10**, 559 (1969).
- [11] E. Krén, E. Nagy, I. Nagy, L. Pál, and P. Szabó, Structures and phase transformations in the Mn-Ni system near equiatomic concentration, *J. Phys. Chem. Solids* **29**, 101 (1968).
- [12] P. Entel, M. E. Gruner, M. Acet, A. Çakır, R. Arróyave, T. Duong, S. Sahoo, S. Fähler, and V. V. Sokolovskiy, Properties and decomposition of Heusler alloys, *Energy Technol.* **6**, 1478 (2018).
- [13] A. Çakır and M. Acet, Shell-ferromagnetism in Ni-Mn-based Heuslers in view of ductile Ni-Mn-Al, *AIP Adv.* **7**, 056424 (2017).
- [14] Z. Wanjiku, A. Çakır, F. Scheibel, U. Wiedwald, M. Farle, and M. Acet, Shell-ferromagnetism and decomposition in off-stoichiometric Ni<sub>50</sub>Mn<sub>50-x</sub>Sb<sub>x</sub> Heuslers, *J. Appl. Phys.* **125**, 043902 (2019).
- [15] A. Çakır, M. Acet, and M. Farle, Shell-ferromagnetism of nano-heuslers generated by segregation under magnetic field, *Sci. Rep.* **6**, 28931 (2016).
- [16] F. Scheibel, D. Spoddig, R. Meckenstock, T. Gottschall, A. Çakır, T. Krenke, M. Farle, O. Gutfleisch, and M. Acet, Room-temperature five-tesla coercivity of a rare-earth-free shell-ferromagnet, *Appl. Phys. Lett.* **110**, 192406 (2017).
- [17] L. Dincklage, F. Scheibel, A. Çakır, M. Farle, and M. Acet, Annealing-time and annealing-temperature dependencies of

- the size of Ni-Mn-In shell-ferromagnetic nano-precipitates by Scherrer analysis, *AIP Adv.* **8**, 025012 (2018).
- [18] E. Wachtel, F. Henninger, and B. Predel, Constitution and magnetic properties of Ni-Mn-Sn alloys-solid and liquid state, *J. Magn. Magn. Mater.* **38**, 305 (1983).
- [19] M. Kök, S. B. Durğun, and E. Özen, Thermal analysis, crystal structure and magnetic properties of Cr-doped Ni-Mn-Sn high-temperature magnetic shape memory alloys, *J. Therm. Anal. Calorim.* **136**, 1147 (2019).
- [20] Y. Martin and H. K. Wickramasinghe, Magnetic imaging by force microscopy with 1000 Å resolution, *Appl. Phys. Lett.* **50**, 1455 (1987).
- [21] V. Cambel, D. Gregušová, P. Eliáš, J. Fedor, I. Kostič, J. Maňka, and P. Ballo, Switching magnetization magnetic force microscopy an alternative to conventional lift-mode MFM, *J. Electr. Eng.* **62**, 37 (2011).
- [22] V. Cambel, M. Precner, J. Fedor, J. Šoltýs, J. Tóbiš, T. Ščepka, and G. Karapetrov, High resolution switching magnetization magnetic force microscopy, *Appl. Phys. Lett.* **102**, 062405 (2013).
- [23] A. Roitburd and G. Kurdjumov, The nature of martensitic transformations, *Mater. Sci. Eng.* **39**, 141 (1979).
- [24] A. Çakır, H. N. Koyun, M. Acet, and M. Farle, Transport properties of shell-ferromagnetic Heusler precipitates in decomposed  $\text{Ni}_{49.8}\text{Mn}_{45.1}\text{Sn}_{5.1}$  and decomposition limit for  $\text{Ni}_{50}\text{Mn}-50-x\text{Sn}_x$  alloys, *J. Magn. Magn. Mater.* **499**, 166265 (2020).
- [25] C. P. Steinmetz, On the law of hysteresis, *Trans. Am. Inst. Electr. Eng.* **IX**, 1 (1892).
- [26] W. H. Meiklejohn and C. P. Bean, New magnetic anisotropy, *Phys. Rev.* **102**, 1413 (1956).
- [27] N. Josten, S. Noorzayee, O. Miroshkina, B. Zingsem, M. Acet, U. Wiedwald, A. Çakır, M. E. Gruner, and M. Farle, Emergence of net magnetization by magnetic field biased diffusion in antiferromagnetic  $L1_0$  NiMn, *Phys. Rev. B* **107**, 174417 (2023).
- [28] E. Hornbogen, Systematics of the cellular precipitation reactions, *Metall. Mater. Trans. B* **3**, 2717 (1972).
- [29] R. Fournelle and J. Clark, The genesis of the cellular precipitation reaction, *Metall. Mater. Trans. B* **3**, 2757 (1972).
- [30] J. Nogués and I. K. Schuller, Exchange bias, *J. Magn. Magn. Mater.* **192**, 203 (1999).
- [31] L. H. Lewis and F. Jiménez-Villacorta, Perspectives on permanent magnetic materials for energy conversion and power generation, *Metall. Mater. Trans. A* **44**, 2 (2013).
- [32] S. Erokhin, D. Berkov, and A. Michels, Micromagnetics of ferromagnetic/antiferromagnetic nanocomposite materials. I. Towards a mesoscopic approach, *Phys. Rev. B* **108**, 214425 (2023).
- [33] S. Erokhin, D. Berkov, and A. Michels, Micromagnetics of ferromagnetic/antiferromagnetic nanocomposite materials. II. Mesoscopic modeling, *Phys. Rev. B* **108**, 214426 (2023).
- [34] H. Ohldag, A. Scholl, F. Nolting, E. Arenholz, S. Maat, A. Young, M. Carey, and J. Stöhr, Correlation between exchange bias and pinned interfacial spins, *Phys. Rev. Lett.* **91**, 017203 (2003).
- [35] U. Nowak, K.-D. Usadel, J. Keller, P. Miltényi, B. Beschoten, and G. Güntherodt, Domain state model for exchange bias. I. theory, *Phys. Rev. B* **66**, 014430 (2002).
- [36] I. K. Schuller, R. Morales, X. Battle, U. Nowak, and G. Güntherodt, Role of the antiferromagnetic bulk spins in exchange bias, *J. Magn. Magn. Mater.* **416**, 2 (2016).
- [37] K. Adachi and C. Wayman, Transformation behavior of nearly stoichiometric Ni-Mn alloys, *Metall. Trans. A* **16**, 1567 (1985).
- [38] L. Pál, T. Tarnóczy, and G. Konczos, Magnetic susceptibility anomaly in nearly equiatomic MnNi alloys, *Phys. Status Solidi B* **42**, 49 (1970).
- [39] N. Josten, O. Miroshkina, M. Acet, M. E. Gruner, and M. Farle, Annealing time, temperature, and field dependence of pinned magnetic moments in the collinear antiferromagnet PdMn, *Phys. Rev. B* **108**, 064417 (2023).
- [40] J. Nogués, T. J. Moran, D. Lederman, I. K. Schuller, and K. Rao, Role of interfacial structure on exchange-biased  $\text{FeF}_2$ -Fe, *Phys. Rev. B* **59**, 6984 (1999).
- [41] L. Zhou, W. Tang, L. Ke, W. Guo, J. D. Poplawsky, I. E. Anderson, and M. J. Kramer, Microstructural and magnetic property evolution with different heat-treatment conditions in an alnico alloy, *Acta Mater.* **133**, 73 (2017).
- [42] W. Gust, Discontinuous precipitation in binary metallic systems, in *Phase Transformations*, Vol. 1 (Institution of Metallurgists, London, 1979), pp. II-27–II-68.